Control of Au nanoantenna emission enhancement of magnetic dipolar emitters by means of VO_2 phase change layers

EMILIJA PETRONIJEVIC,[1,*] MARCO CENTINI,[1] TIZIANA CESCA,[2] GIOVANNI MATTEI,[2] FABIO ANTONIO BOVINO,[1] AND CONCITA SIBILIA[1]

[1]*Sapienza University of Rome Department S.B.A.I., Via A. Scarpa 14, I-00161 Rome, Italy*
[2]*University of Padova, Physics and Astronomy Department, Via Marzolo 8, I-35131 Padova, Italy*
**emilija.petronijevic@uniroma1.it*

Abstract: Active, ultra-fast external control of the emission properties at the nanoscale is of great interest for chip-scale, tunable and efficient nanophotonics. Here we investigated the emission control of dipolar emitters coupled to a nanostructure made of an Au nanoantenna, and a thin vanadium dioxide (VO_2) layer that changes from semiconductor to metallic state. If the emitters are sandwiched between the nanoantenna and the VO_2 layer, the enhancement and/or suppression of the nanostructure's magnetic dipole resonance enabled by the phase change behavior of the VO_2 layer can provide a high contrast ratio of the emission efficiency. We show that a single nanoantenna can provide high magnetic field in the emission layer when VO_2 is metallic, leading to high emission of the magnetic dipoles; this emission is then lowered when VO_2 switches back to semiconductor. We finally optimized the contrast ratio by considering different orientation, distribution and nature of the dipoles, as well as the influence of a periodic Au nanoantenna pattern. As an example of a possible application, the design is optimized for the active control of an Er^{3+} doped SiO_2 emission layer. The combination of the emission efficiency increase due to the plasmonic nanoantenna resonances and the ultra-fast contrast control due to the phase-changing medium can have important applications in tunable efficient light sources and their nanoscale integration.

1. Introduction

One of the main goals of modern nanophotonics is the use of optical nanocomponents as building blocks of integrated circuits for applications in future computers and information systems. However, there is still a lack of chip-scale light sources and optical amplifiers with large bandwidths and high energy efficiencies, as well as active components that allow for efficient high-speed light modulation. Rare earth-based approaches offer unique advantages with respect to semiconductor optical components such as long carrier lifetimes, and longer quantum coherence times [1]. For example, an erbium-doped waveguide amplifier has been shown to work at a modulation speed higher than 170 Gbit/s [2]. Moreover, erbium-based materials are preferred to semiconductors in quantum information systems due to their emission at telecommunication wavelengths with sharp spectral features. However, even though they have high quantum efficiencies, their excitation cross-sections are very low, while for nanoscale integration, erbium-based materials with much higher gain are required. Attempts to increase the optical gain by increasing the doping density encountered other negative effects, such as concentration-related quenching due to clustering or interaction of erbium atoms when above the critical density [3]. Instead, the emission efficiency can be enhanced by putting the emitters in the near-field of nanostructures designed to have resonances that match the wavelength of excitation or emission [4-9]. Another issue is to combine efficiency and modulation speed by dynamical manipulation of the local density of states. As the process of light emission depends both on the optical environment and on the intrinsic properties of the

emitter, a fast modulation of the environment properties can produce a fast modulation of the local density of states and field localization resulting in a fast (sub-lifetime) emission modulation [10].

In this work, we combined the enhancement of a dipolar emitter emission due to the proximity of a resonant nanostructure, and the possibility to modulate it by means of a thin layer of a phase change material (PCM). PCMs have been used as active subwavelength elements that can switch between phases that differ in electric and optical properties. The phase change results in a modulation of amplitude or phase of transmission or reflection over nanoscale propagation lengths, and it is compatible with fast optical systems [11-18]. Vanadium dioxide (VO_2) is a promising candidate for nanoscale modulation since it shows dramatic contrast in the complex refractive index as it undergoes a structural phase transition from monoclinic (semiconductor) to rutile (metallic) phase at ~68°C [15] (Figs. 1(a)-1(b)). The phase change can be induced thermally, electrically or optically, and it has been shown to provide tuning of the resonances of the nanostructured materials [16-18]. Moreover, it has been shown that optically induced phase change transition in VO_2 can be achieved in the fs time scale making it a perfect candidate material for ultra-fast optical switching and modulation [19,20].

The structure under examination is shown in Fig. 1(c): a thin VO_2 layer is deposited on a glass substrate, and covered by a thin spacer layer of silica, which is doped by luminescent ions; above the spacer, Au nanoantennas are added to provide the plasmonic resonant enhancement. Sandwiched magnetic dipoles feel strong resonance when VO_2 is metallic (hot state) due to the strong magnetic field arising from the current loops between the Au nanoantenna and the VO_2 layer; this resonance blue-shifts and decreases when VO_2 is in the semiconductor (cold) state. We first studied the absorption properties and magnetic field confinement effects for a single Au nanoantenna – SiO_2 – VO_2 structure; the geometric parameters are chosen to set the maximum absorption at the 1540 nm emission line of Er^{3+} ions when VO_2 is metallic. We then investigated the influence of the VO_2 phase change on the emission of single dipoles in the layer under the nanoantenna, considering different positions, types (i.e. magnetic or electric dipole), and orientations. We show that the emitted far-field of resonant magnetic dipoles [21,22] follows the VO_2 phase change contrast. We finally optimized the structure for the highest emission contrast and provide the sensitivity analysis of the geometric parameters' margins. This study is of particular importance due to the mixed nature of Er^{3+} transition at 1540 nm, where both electric and magnetic dipole components are of the same order of magnitude [23-25]: a resonant magnetic field can be used to enhance the corresponding transition, and switch it by means of PCM.

2. Plane-wave excitation

A single Au nanorod acts as a nanoantenna, with an electric dipole resonance when the incident electric field is parallel to its long axis [26,27]. High field localization and high local density of states at the resonance can modify the emission rates of electric dipoles [28]. However, if the dielectric substrate is interrupted by a close metallic layer, another type of resonance can occur: a current loop formed between the nanoantenna and the metal below induces a high magnetic field in the dielectric, leading to a magnetic resonance [29,30]. Our hybrid structure, Fig. 1(c), has similar features when the emitting layer is thin enough to allow for the loop formation due to the induced "mirror" charge from the nanoantenna to the metallic layer, providing enhanced metal-insulator-metal (MIM) absorption when VO_2 is heated to its metallic state; this resonant behavior vanishes when VO_2 is cooled down to its semiconductor state. VO_2 was recently proposed for the high contrast switching of the resonant absorption in MIM metamaterials [18,31-33]. In the present work, we used a commercial-grade simulator based on the 3D Finite Difference Time Domain (FDTD) method in Lumerical [34] to investigate the optical response in a system consisting of an Au nanoantenna of length L, width W and thickness t, standing upon a t_{em} thick Er-doped SiO_2 layer and a t_{pc} thick VO_2 layer on a silica substrate (see Appendix

A). All the simulations consider two stable states of VO_2, while the study of the temporal dynamics of its switching is out of the scope of this work. It is worth underlining that the induced heating that changes the phase of the VO_2 layer can be also optical [10], by means of another "control" laser that is not resonant with the Er^{3+} excitation or emission (e.g. at 1064 nm). The geometric parameters can be chosen to give the resonance for the hot VO_2 state at the 1540 nm emission of Er^{3+}; we thus use plane-wave excitation with *x*-polarized total-field-scattered-field (TFSF) source (see Appendix B) to find the resonance of the absorption cross-section σ_{abs}. The absorption efficiency is defined as $\eta=\sigma_{abs}/\sigma_{Au}$ [35], where $\sigma_{Au}=W\cdot L$ is the nanoantenna footprint. Figure 1(d) shows the values of η for the two VO_2 states, cold (blue line) and hot (red line), for L=340 nm, W=50 nm, t=40 nm, t_{em}=50 nm, and t_{pc}=60 nm. Around 1540 nm there is a strong resonance for the hot state; however, one should note that a lower, blue-shifted resonance still exist in the cold state, even though there is no metal to form the current loop. This is due to the fact that in the cold state, VO_2 is a high refractive index semiconductor in this spectral range (Fig. 1(a)), providing the magnetic response due to the displacement currents. In Fig. 1(e) we show the magnetic field intensity distribution at 1540 nm determined by collecting the field from a *xz* cross-section monitor: as expected, a much higher magnetic field confinement and enhancement are present in the hot state.

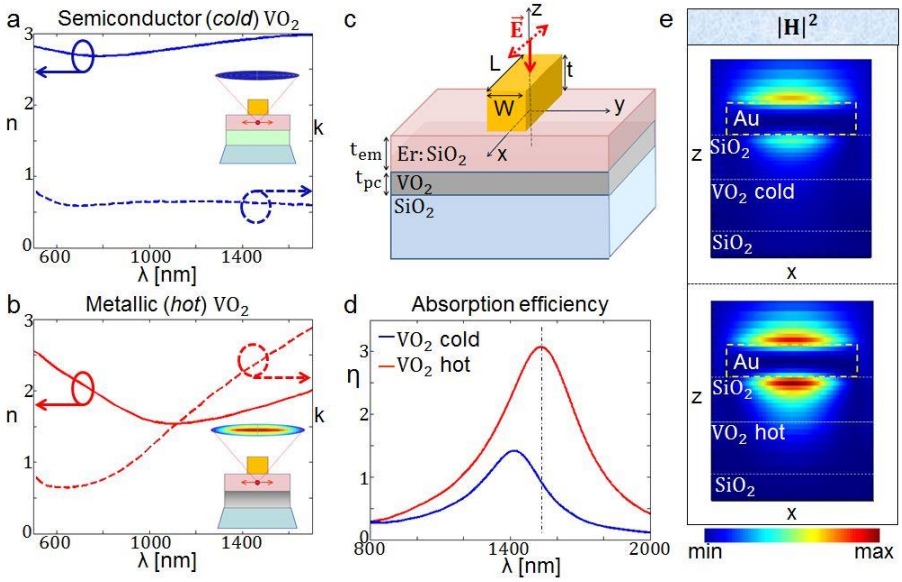

Fig. 1. Complex refractive indices [10] of VO_2 in (a) semiconductor (cold), and (b) metallic (hot) state. Insets show the principle of magnetic dipole emission control (low and high emission in cold and hot state, respectively). (c) Schematic of the investigated hybrid nanostructure: the Au nanoantenna is defined by its length L, width W and thickness t, and it lies above a multilayer structure, made of t_{em} thick Er:SiO_2, and t_{pc} thick VO_2 layers upon SiO_2 substrate. (d,e) *x*-polarized plane-wave simulations for the two VO_2 states; the parameters of the nanostructure are L=340 nm, W=50 nm, t=40 nm, t_{em}=50 nm, and t_{pc}=60 nm: (d) absorption efficiency, and (e) magnetic field intensity at 1540 nm, monitored in *xz* cross-section, at y=0 nm.

As the dipolar emitters are to be inserted in the region under the nanoantenna, we studied the magnetic field enhancement in the center of the simulation region, at Δz=-10 nm. In Fig. 2(a) we show the spectra of the magnetic field intensity, normalized to the one of the incident plane-wave (without the nanostructure) H_0: for both states the magnetic enhancement spectrally coincides with the absorption resonant behavior previously shown. For *x*-polarized excitation the magnetic field is *y*-oriented; in Fig. 2(b) the *yz* cross-section (*x*=0 nm) shows the enhancement of this component at 1540 nm, which reaches 100 under the nanoantenna in the hot state.

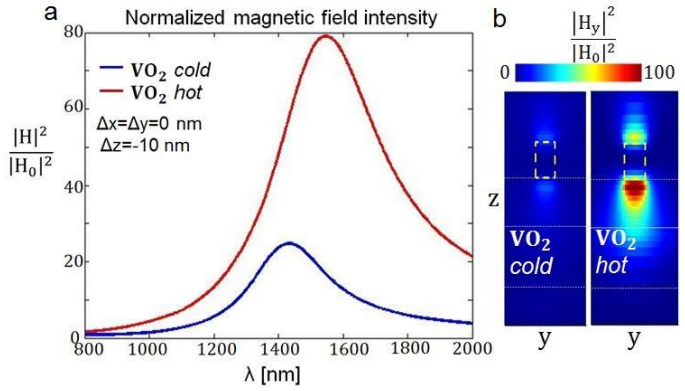

Fig. 2. (a) Spectral dependence of the magnetic field intensity normalized to the intensity of the incident magnetic field H_0, at the point $\Delta x=\Delta y=0$ nm, $\Delta z=-10$ nm, for the two VO_2 states. (b) Normalized H_y intensity for the two VO_2 states at 1540 nm, monitored in *yz* cross-section, at $x=0$ nm.

3. Dipole excitation

Magnetic dipole emission enhancement of rare-earth metal ions has been investigated in resonant plasmonic [36-40] and dielectric [41,42] nanostructures. Thus, we further investigated how the enhancement due to the magnetic resonance influences a perfect dipole (without nonradiative decays). To do this, first we placed a broadband magnetic dipole source centrally, at the distance $\Delta z=-10$ nm under the nanoantenna, and monitored the power emitted in the positive *z* half-space, as illustrated in Fig. 3(a); θ and φ are the emission cone half-angle, and azimuthal angle, respectively. In this way, we investigated how the total power spectrum changes with the change of the VO_2 phase; the results have been calculated as $T \cdot P_{source}$ (See Appendix C). As expected, only the *y*-oriented dipoles spectrally follow the resonances seen in the absorption and magnetic field, Fig. 3(b). Since the emission contrast between the two states arises from the sum of the three dipole orientations, the emission of *x*-oriented dipoles will eventually lower the overall contrast, while the emission of *z*-oriented dipoles is negligible. It is worth noting that if we change the dipole type from magnetic to electric, the resonance is expected for the dipole orientation along the electric field, i.e. in *x* direction: indeed, we note some resonant behavior in both states for *x*-oriented electric dipoles, Fig. 3(c).

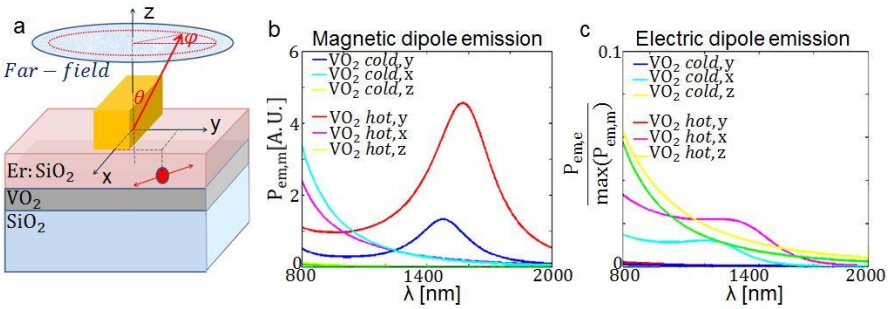

Fig. 3. (a) Sketch of the dipole excitation simulations. θ and φ are the emission cone half-angle, and azimuthal angle, respectively. (b-c) Spectra of the total power emitted to z^+ far-field for the two VO_2 states, for different dipole orientations of a dipole located at the center ($\Delta x=\Delta y=0$ nm), at $\Delta z=-10$ nm, for (b) magnetic dipole; (c) electric dipole.

The strongest emission $\max(P_{em,m,y})$ for *y*-oriented magnetic dipoles is at the wavelength of the highest magnetic field in the hot state, i.e. at 1540 nm. In order to compare this optimal emission to the cases where the dipole is placed farther from the nanoantenna center, we fixed the emission wavelength at 1540 nm, and monitored the emitted power as a function of the

dipole's displacement. Figure 4(a) shows results for the two states as a function of |Δx| or |Δy|, keeping |Δy|=0 nm or |Δx|=0 nm, respectively. Figure 4(b) shows the dependence on |Δz| while keeping |Δx|=|Δy|=0 nm. The normalized power follows the spatial dependence of the magnetic field shown in Figs. 1(e) and 2(b).

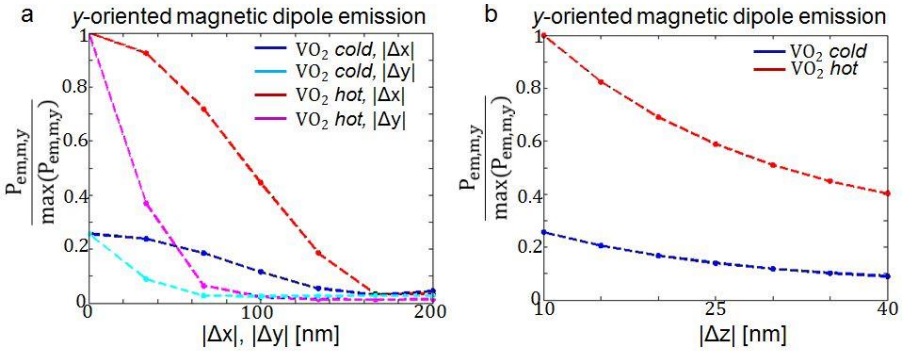

Fig. 4. Normalized total power emitted at 1540 nm for a *y*-oriented dipole, positioned (a) at Δz=-10 nm, as a function of the distance from the center |Δx| or |Δy|, and (b) at Δx=Δy=0 nm, as a function of |Δz|. The power is normalized to the maximum power emitted for the resonant dipole at 1540 nm (*y*-oriented dipole and the hot VO_2 state).

We then addressed the change in the far-field distribution of the emission by calculating it for a magnetic dipole at 1540 nm placing a near-field monitor above the nanoantenna (see Appendix D). Figure 5(a) shows that a *y*-oriented dipole emits most efficiently at 1540 nm for the hot state. In order to account for the random orientation of the dipoles, in Fig. 5(b) we show the average far-field distribution, calculated by summing and averaging the far-field power from three simulations with x, y and z-oriented dipoles radiating at 1540 nm (the dipole is placed centrally at |Δx|=|Δy|=0 nm and Δz=-10 nm). A notable high contrast between the states was demonstrated, especially close to normal incidence. However, this contrast will be effectively lowered once the dipole is positioned farther from the center (where the designed structure enhances the magnetic response). Possible solutions to prevent this decrease are to pattern the distribution of the emitters in the SiO_2 spacer volume under the nanoantenna, or to simultaneously use excitation enhancement [43] to tailor the magnetic field which can increase the resonant magnetic contribution of the dipoles away from the center. Anyhow, for the out-coupling efficiency of the design, one should consider the emitters deposited over the SiO_2 volume, and calculate the contrast between the two states only after averaging over many possible positions. Therefore, in the following we investigated a magnetic dipole distribution below periodically patterned Au nanoantennas, providing a path to metamaterial-PCM governed tunable emission.

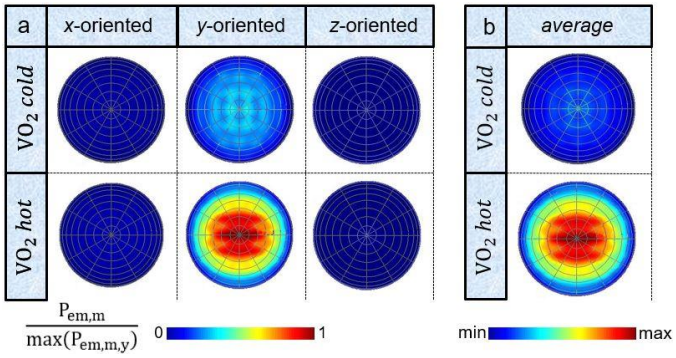

Fig. 5. (a) Distribution of power emitted to the z^+ far-field, for a magnetic dipole at 1540 nm, in the two VO_2 states and three different dipole orientations. The dipole is located at the center, at Δz=-10 nm. All the maps are normalized to the maximum value (power emitted to far-field $\theta=\varphi=0$ for the y-oriented dipole in the hot state). (b) Far-field emission distribution above the structure, averaged over the three orientations of the magnetic dipole which is positioned centrally at Δz=-10 nm, and emits at 1540 nm.

4. Periodic structure

Coupling of the emitters with periodic nanostructures has recently proven to provide emission rate modification and quantum efficiency enhancement [9]. Here we investigate the coupling of a magnetic emitter with a metamaterial, comprising a 2D array of Au nanoantennas with periodicity p in both *x*- and *y*-directions, as shown in Fig. 6(a); the geometric parameters of the nanoantennas and the layers below are kept the same as in the previous section. In Appendix E we perform plane-wave simulations with periodic boundary conditions (PBCs) in *xy* plane to explore the magnetic resonance in the metamaterial; as it remains governed by the behavior of the single nanoantenna, we further choose periodicities with higher absorption contrast between the two VO_2 states. Next, we study the emission response of dipoles under the metamaterial. In the dipole excitation case, spontaneous emission cannot be modelled by applying PBCs as it would lead to incorrectly induced coherence of the sources. Instead, we replicate the unit cells in the FDTD volume already defined in Appendix D, which now includes more than 100 unit cells. We first consider magnetic dipoles homogenously positioned in a unit cell at Δz=-10 nm, emitting at 1540 nm. The emitted far-field is averaged over the three dipole orientations and 72 dipole positions. The symmetry of the structure then reduces this number to 16, as indicated by the green dots in Fig. 6(a); for the dipoles shared by 2 and 4 unit cells, the emitted power is scaled by factors 0.5 and 0.25, respectively. The simulation domain contains at least 100 unit cells. Figure 6(b) shows the far-field emitted power for p=900 nm and p=800 nm, normalized to the maximum value for the hot state (i.e. for $\theta=\varphi=0$) for a homogeneous distribution of emitters in the unit cell, for the two VO_2 states. The period decrease enhances the coupling between adjacent nanoantennas especially in *x*-direction; this effectively leads to a lower directivity in the hot state, and to even a lower overall contrast at $\theta=0$. More importantly, the emitted far-field distribution differs for the two states, but the overall contrast is dramatically lowered with respect to the one of the centrally positioned dipoles in Fig. 5(b). This is due to the detrimental contribution of dipoles positioned farther from the center; namely, Fig. 4(a) shows that the dipoles positioned at $|\Delta y|>60$ nm do emit less due to a lower magnetic enhancement, but for the two states there is almost no contrast, and the same applies for the dipoles at $|\Delta x|>160$ nm. Such low far-field contrast is obtained for the dipoles positioned at the borders and corners of the structure; in Fig. 6(c) the far-field emission of such dipoles for the two states is shown.

In order to optimize the far-field contrast, in Fig. 6(d) only contributions from the emitters under the nanoantenna are averaged ($|\Delta x|<L/2$ and $|\Delta y|<W/2$). This approach greatly enhances the difference between the far-field distribution of the two states, enabling a strong emission and its directivity around $\theta=0$ in the hot state, which vanishes when switching to the cold state. Therefore, the smart positioning of the emitting material under the nanoantennas can provide the overlap of the dipole distribution with the points of high magnetic field enhancement in the hot state (Figs. 1(e) and 2(b)), and high magnetic field contrast between the two states; this in turns leads to a better far-field emission contrast. Such structures can be fabricated by patterning the dipole distribution under the nanoantennas, for example, by ion implantation through masks before the Au nanoantenna metamaterial fabrication step.

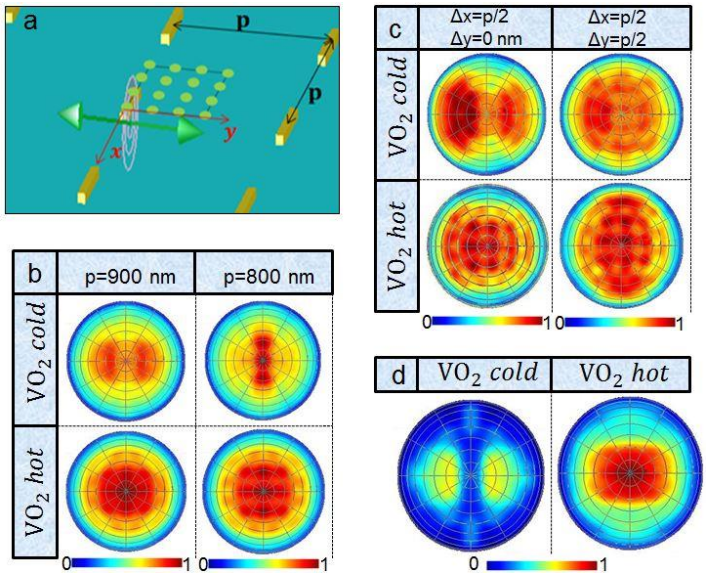

Fig. 6. (a) Simulation sketch for a periodic structure, with dipoles positioned in a unit cell (green dots). (b) Far-field averaged over the three dipole orientations with homogeneous distribution in the unit cell at Δz=-10 nm, for p=900 nm, and p=800 nm. (c) Far-field response of the dipoles positioned away from the center for both VO_2 states. The randomly oriented magnetic dipole is positioned at (left) the border and (right) the corner of the unit cell. (d) Far-field averaged over the three dipole orientations and positions in the unit cell (*xy* plane) at Δz=-10 nm, with dipoles only under the nanoantennas (patterned distribution). All maps are normalized to the hot state maximum.

In the following, we quantified the far-field emission contrast between the two states, and investigated its dependence on periodicity and far-field collection angle. The radiative decay rate enhancement γ_{rad} can be calculated as the ratio of the total power radiated to the far-field P_{rad} and the power that would be radiated from the same dipole in the homogeneous medium P_0. The quantum efficiency QE, instead, is usually defined as the ratio of P_{rad} to the power radiated by the dipole. In the investigated structure, however, both γ_{rad} and QE are greater in the cold state as a large part of the power is transmitted through VO_2 in the semiconductor state, while metallic VO_2 introduces more absorption losses. Thus, we define the far-field directional efficiency as:

$$\gamma_{ff} = \frac{P_\theta}{P_{rad}} = \frac{\sum_{|\Delta x|,|\Delta y|} \int_{ff(\theta)} P \cdot ds(\theta)}{\sum_{|\Delta x|,|\Delta y|} (\int_{z+} P \cdot ds + \int_{z-} P \cdot ds)}, \quad (1)$$

which represents the part of the total radiated power P_{rad} which is radiated into a cone of semi-aperture θ in z^+ direction (red dashed circle in Fig. 3(a)). The summation is done for 15 different positions under the nanoantenna, and for three magnetic dipole orientations, at Δz=-10 nm. In Fig. 7 we show the γ_{ff} contrast ($\gamma_{ff,hot}/\gamma_{ff,cold}$) for the two states as a function of the periodicity p and collection angle θ. As expected, γ_{ff} is always higher for the hot state, and, in accordance with the emission directionality of the hot state, the contrast decreases with the increasing of θ, except for the lowest investigated p=800 nm, in agreement with Fig. 6(b). This is very likely due to the higher neighbor nanoantenna coupling for lower p, which leads to lower directionality, inverts the $\gamma_{ff,hot}/\gamma_{ff,cold}$ θ dependence and finally leads to much lower γ_{ff} contrast. For p>800 nm, there is a high directionality; for example, if a low numerical aperture (NA) is chosen for the signal collection, i.e. θ=10°, then for p=1000 nm $\gamma_{ff,hot}/\gamma_{ff,cold}$>9. The contrast is lowered for p=950 nm due to the increased $\gamma_{ff,cold}$ for this periodicity. Therefore, VO_2 can be used to modulate the far-field efficiency of the designed metamaterial, and the contrast can be

optimized by means of periodicity tuning. It should be noted that, for all θ, VO_2 switching from the hot to the cold state leads to γ_{ff} decrease both because of the lower power radiated around θ=0°, and because of the increase of P_{rad}, as the power emitted to the z^- far-field is higher in the cold state.

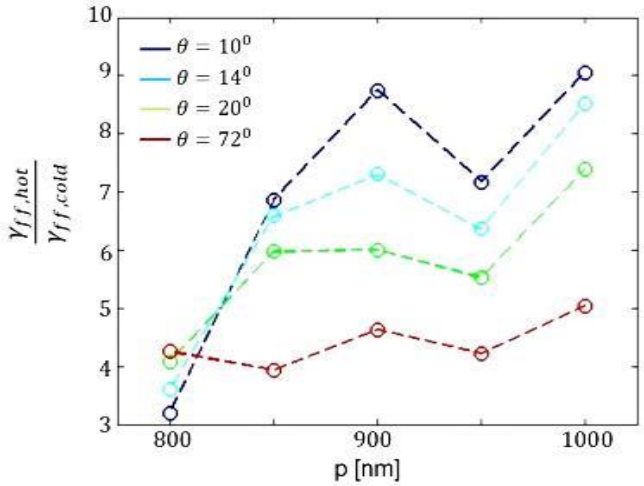

Fig. 7. Far-field directional efficiency ratio $\gamma_{ff,hot}/\gamma_{ff,cold}$ for the two states as a function of p and collection angle θ for a distribution of randomly oriented magnetic dipoles positioned under the nanoantennas, at Δz=-10 nm.

As this design was optimized for the z^+ far-field contrast, we further defined figure of merits of the contrast which include the emitted power that would be collected in a real experiment with collection angle θ; in Table 1 we calculated the normalized modulation depth (MD) efficiency and the contrast ratio (CR) as:

$$MD = 100 \cdot \frac{P_{\theta,hot} - P_{\theta,cold}}{P_{\theta,hot} + P_{\theta,cold}}, CR = \frac{P_{\theta,hot}}{P_{\theta,cold}}. \quad (2)$$

Again, for p=800 nm, CR and MD are the lowest for all collection angles; the nanostructure's contrast was optimized for the single nanoantenna response, so in this design lower p values should be avoided. For high NA, MD and CR drop because of the two lobes present in the cold state (Fig. 6(b)). Finally, the metamaterial with p=850 nm gives the highest directional contrast ratio for θ=10°: MD~69, CR~5.5.

Table 1. Modulation depth (MD) and contrast ratio (CR) for different p and collection angles θ.

p[nm]	MD [10°]	CR [10°]	MD [14°]	CR [14°]	MD [20°]	CR [20°]	MD [72°]	CR [72°]
800	13	1.3	21	1.5	27	1.7	28	1.8
850	69	5.5	67	5.1	64	4.6	51	3
900	56	3.5	48	2.9	40	2.3	29	1.8
950	68	5.3	64	4.6	60	4.1	51	3
1000	54	3.3	52	3.1	47	2.8	31	1.9

In addition to the dipole patterning in the *xy* plane, we investigated the influence of positioning the set of dipoles in *z*-direction; the calculations have been done for p=900 nm, which provides high normalized absorption modulation depth (see Appendix E). In Table 2

these values are calculated for the same collection angles as before, and only a slight decrease is noted moving the dipole plane deeper in the SiO_2 layer. Total MD and CR are then calculated by summing contributions from all randomly oriented dipoles where $|\Delta x| \leq L/2$, $|\Delta y| \leq W/2$, and $-40\ \text{nm} \leq \Delta z \leq -10\ \text{nm}$. Even though a deeper distribution emits less power (as expected from Fig. 4(b)), this does not significantly influence the overall contrast, Fig. 8. Therefore, a distribution of dipoles in the range $-40\ \text{nm} < z < -10\ \text{nm}$ is expected to provide a similar far-field contrast between the two states.

Table 2. Modulation depth (MD) and contrast ratio (CR) for the set of dipoles under the nanoantenna for p=900 nm, at different Δz and collection angles θ.

Δz [nm]	MD [10°]	CR [10°]	MD [14°]	CR [14°]	MD [20°]	CR [20°]	MD [72°]	CR [72°]
-10	56	3.5	48	2.9	40	2.3	29	1.8
-20	53	3.3	47	2.8	40	2.3	29	1.8
-30	50	3	45	2.6	39	2.3	29	1.8
-40	48	2.8	43	2.5	37	2.2	28	1.8
total	52	3.2	47	2.7	39	2.3	29	1.8

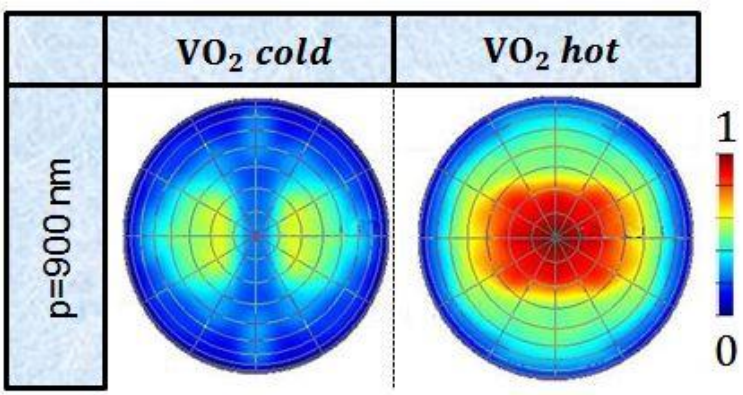

Fig. 8. Far-field power averaged over the three orientations and dipole positions for which $|\Delta x| \leq L/2$, $|\Delta y| \leq W/2$, and $-40\ \text{nm} \leq \Delta z \leq -10\ \text{nm}$, for the nanoantenna metamaterial with p=900 nm at 1540 nm. Both maps are normalized to the hot state maximum (θ=φ=0).

Finally, we performed the sensitivity analysis of the design, by simulating the resonant magnetic field contrast as a function of Gaussian distributions of the parameters in the (L-W-t-t_{pc}) parameter space (see Appendix F). As the resonances are spectrally wide, we can conclude that the contrast ratio is rather stable with respect to changes in the geometrical parameters of the nanostructure and thus the designed device is expected to have a good stability with respect to fabrication tolerances.

5. Conclusion

In the present work we demonstrated that the combination of a phase-change material and a plasmonic nanostructure can be effectively used to externally modulate the emission of magnetic dipoles. Particularly, we have shown that a hybrid nanostructure consisting of magnetic dipoles sandwiched between an Au nanoantenna array and a multilayer structure containing VO_2 can lead to efficient modulation of the Er^{3+} emission at 1540 nm. This is due to the control of intensity and spectral position of the magnetic resonance of the overall structure, which change with VO_2 changing from semiconductor to metallic state upon an

external stimulus (which can be thermal, electrical or optical). In the present work, the nanostructure is optimized to give enhanced magnetic field in the layer between the nanoantenna and VO_2 at 1540 nm when VO_2 is metallic. We showed that the high magnetic field contrast between the two states of the VO_2 layer leads to a similar emission contrast of the magnetic dipoles, thus controlling the difference in the far-field collected signal between the two states. Moreover, the arrangement of the Au nanoantennas in a 2D array and the periodic pattering of the distribution of emitters lead to high values of modulation depth and contrast ratio between the two states for magnetic emission of Er^{3+}; these values can be optimized by choosing the right periodicity and collection angle. We believe that such an approach can be of great importance for the realization of efficient light sources at the nanoscale, where the optically induced phase transition of VO_2 can enable the ultrafast modulation.

Appendix A: Simulation and material properties

In order to simulate the absorption and emission properties of the investigated nanostructure, a single Au nanoantenna, or a 2D periodic array of nanoantennas, is designed upon two thin layers (Er:SiO_2 and VO_2) and a semi-infinite substrate, all of which are infinite in the *xy* plane. The simulation region is defined by putting perfectly matched layers (PMLs) in all six directions. PMLs are at least half the maximum wavelength distant from the nanoantenna and the lowest VO2 *z* coordinate to prevent reflection of the evanescent fields. We assumed both SiO_2 substrate and Er:SiO_2 emitting layer to be lossless (n=1.46), which is justified for doping with low concentrations of photoluminescent ions. The optical properties of Au are taken from the Lumerical database (Johnson&Christy), while for VO_2 we used recently measured complex refractive index values [10], fitted in the wavelength range 800-2000 nm.

Appendix B: Plane-wave single nanoantenna absorption

In order to discriminate the total field region from the one with the scattered field, a total-field scattered source (TFSF) is used to illuminate the nanoantenna along its long axis, i.e. *x*-direction. The absorption cross-section is then calculated by surrounding the nanoantenna with a box in the total field region, "inside" the TFSF source. This built-in box in Lumerical uses six 2D monitors to calculate the power flow in the box across the spectral range. The parameters of the final design were chosen to provide high contrast between the two VO_2 states at 1540 nm.

Appendix C: Emitted power of dipole excitation

An oscillating dipole acts as a point source of electromagnetic fields in FDTD simulations; the base amplitude is defined to give 1 fW radiated power in the simulation domain. The modulation of the emission by means of VO_2 is investigated by considering the power emitted by the dipole in the positive *z* direction, as could be of interest in a future experiment (in the opposite direction VO_2 losses are detrimental for the dipole efficiency). A perfect dipole source is put in the region under the nanoantenna, and the spectral response of the structure is monitored in the 800-2000 nm range. The simulation region is again defined by six PMLs. Below the upper *z* PML boundary, a transmission monitor is placed to measure the total radiation in the same range; the simulation parameters are fixed for the two VO_2 states. Here special attention must be made to the normalization of the power. Namely, the results of the transmission function T are by default normalized to the source power that would be emitted by the same dipole in a homogeneous medium. However, the actual radiated power (dipole power) strongly depends on the environment, hence the real transmitted percentage in a given direction needs to be normalized as $T*P_{source}/P_{dipole}$. Here we are interested in how the total power spectrum changes with the change of VO_2 phase, hence we present results calculated as $T*P_{source}$[A.U.].

Appendix D: Far-field of dipole excitation

For the far-field distribution calculations, a frequency-domain field-profile monitor placed 10 nm above the nanoantenna collects the near-field data and decomposes it in a basis of plane waves propagating at different angles; the result is then expressed as the far-field radiation intensity in angles (θ,φ). For the far-field efficiency calculations, another field-profile monitor is placed 10 nm under the lowest z boundary of the VO_2 layer. The total power emitted to the far-field is calculated from the integration of the far-field power projected from these two monitors. The size of the FDTD domain is set to 10 μm x 10 μm, which is large enough so that there is no electric field at the borders of the near-field monitor. In the far-field plots, white circles correspond to θ change with 10° step, while white lines mark φ with 30° step.

Appendix E: Plane-wave nanoantenna metamaterial absorption

Here we use an *x*-polarized plane-wave under normal incidence, Fig. 9(a), and define PBCs in *xy* plane, while keeping PMLs in *z*-direction. We calculate the total absorption by surrounding the nanoantennas with a box of monitors, calculating the power density, and integrating it over the volume. This way one gets the total power absorbed in that part of the structure, normalized to the total power of the source; the source has the electric field amplitude of 1V/m. In Fig. 9(b) we see the same localized resonance at around 1540 nm (its position does not depend on p). In Fig. 9(c), in the cold state the resonance linearly red-shifts with p, suggesting a surface lattice nature of the mode. Finally, in Fig. 9(d) we investigate the normalized absorption modulation depth defined as:

$$MD_A = 100 \cdot \frac{A_{hot} - A_{cold}}{A_{hot} + A_{cold}}. \qquad \text{(E1)}$$

This figure of merit shows an enhancement with respect to the nonperiodic structure (from Fig. 1(d) in the main manuscript, this value is ~53). This can be understood in terms of an effective surface for the magnetic resonance: for the cold state, for periods greater than 800 nm the localized contribution due to the magnetic resonance almost disappears as such structure has no metallic structure below, and the volume of the nanoantenna compared to the unit cell becomes too low to support it. This is not the case for the hot state, where the magnetic resonance still exists for larger periods because of the metallic layer below. Therefore, in the main manuscript we investigated periods in the range 800-1000 nm.

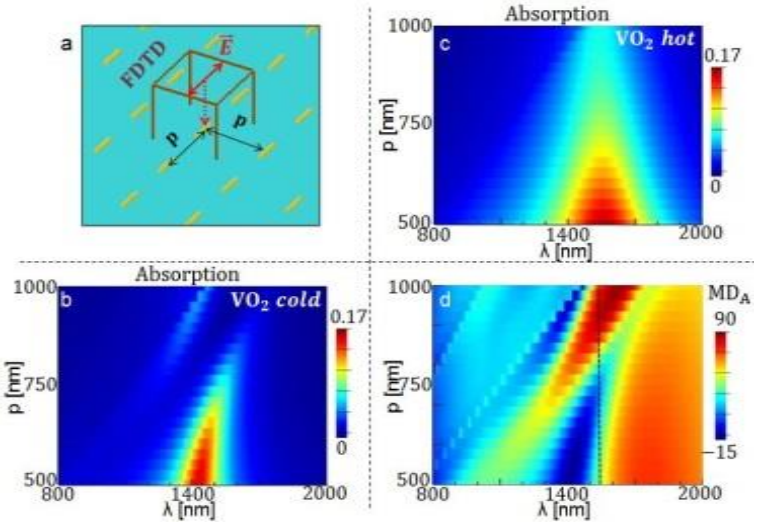

Fig. 9. (a) Sketch of the periodic structure. (b) Absorption dependence on the period when VO_2 is *hot* and (c) when VO_2 is *cold*. (d) Normalized absorption modulation depth dependence on the period.

Appendix F: Sensitivity analysis

In order to evaluate the sensitivity of the design with respect to change in the geometric parameters of the system, we suppose that the sensitivity of emission will follow the sensitivity of absorption, and perform 800 simulations in the (L-W-t-t_{pc}) parameter space for the two states, and p=900 nm. We take the following Gaussian distributions: L=340±5 nm, t_{pc} =60±5 nm, t=40±2 nm, and W=50±2 nm. We confirm that the normalized absorption MD always lies around 75%, as expected from Fig. 9(d).

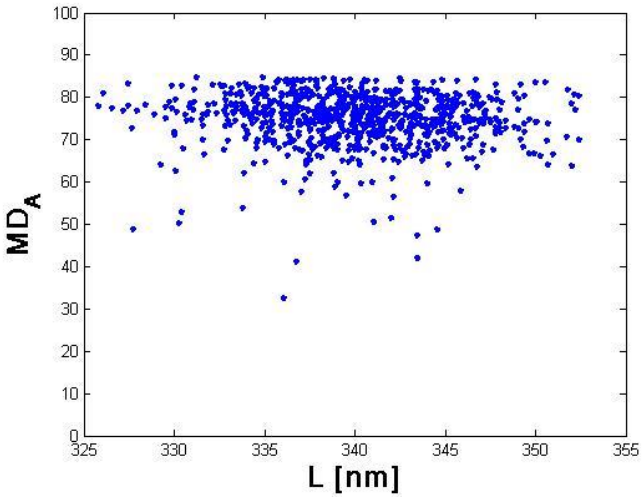

Fig. 10. Scatter plot of MD_A as a function of manufacturing tolerances of the parameter L. The device parameters are taken as Gaussian distributions defined as: L=340±5 nm, t_{pc}=60±5 nm, t=40±2 nm, and W=50±2 nm.

References

1. H. Sun, L. Yin, Z. Liu, Y. Zheng, F. Fan, S. Zhao, X. Feng, T. Li, and C. Z. Ning, "Giant optical gain in a single-crystal erbium chloride silicate nanowire," Nat. Photonics **11**(9), 589-593 (2017).
2. J. Bradley, M. Costa e Silva, M. Gay, L. Bramerie, A. Driessen, K. Wörhoff, J. Simon, and M. Pollnau, "170 GBit/s transmission in an erbium-doped waveguide amplifier on silicon," Opt. Express **17**(24), 22201–22208 (2009).
3. E. Snoeks, P. G. Kik, and A. Polman, "Concentration quenching in erbium implanted alkali silicate glasses," Opt. Mater. **5**, 159-167 (1996).
4. H. Mertens and A. Polman, "Plasmon-enhanced erbium luminescence," Appl. Phys. Lett. **89**, 211107 (2006).
5. Y. Gong, S. Yerci, R. Li, L. Negro, and J. Vučković, "Enhanced light emission from erbium doped silicon nitride in plasmonic metal-insulator-metal structures," Opt. Express **17**(23), 20642-20650 (2009).
6. T. Cesca, B. Kalinic, N. Michieli, C. Maurizio, A. Trapananti, C. Scian, G. Battaglin, P. Mazzoldi, and G. Mattei, "Au–Ag nanoalloy molecule-like clusters for enhanced quantum efficiency emission of Er^{3+} ions in silica," Phys. Chem. Chem. Phys. **17**, 28262-28269 (2015).
7. T. Cesca, B. Kalinic, C. Maurizio, C. Scian, G. Battaglin, P. Mazzoldi, and G. Mattei, "Interatomic coupling of Au molecular clusters and Er^{3+} ions in silica," ACS Photonics **2**(1), 96-104 (2015).
8. B. Kalinic, T. Cesca, C. Scian, N. Michieli, I. G. Balasa, E. Trave, and G. Mattei, "Emission efficiency enhancement of Er^{3+} ions in silica by near-field coupling with plasmonic and pre-plasmonic nanostructures," Phys. Status Solidi A **215**, 1700437 (2018).
9. N. Michieli, B. Kalinic, C. Scian, T. Cesca, and G. Mattei, "Emission rate modification and quantum efficiency enhancement of Er^{3+} emitters by near-field coupling with nanohole arrays," ACS Photonics **5**(6), 2189-2199 (2018).

10. S. Cueff, D. Li, Y. Zhou, F. J. Wong, J. A. Kurvits, S. Ramanathan, and R. Zia, "Dynamic control of light emission faster than the lifetime limit using VO_2 phase-change," Nat. Commun. **6**, 8636 (2015).
11. B. Gholipour, J. Zhang, K. F. MacDonald, D. W. Hewak, and N. I. Zheludev, "An all-optical, non-volatile, bidirectional, phase-change meta-switch," Adv. Mater. **25**(22), 3050–3054 (2013).
12. M. Rudé, V. Mkhitaryan, A. E. Cetin, T. A. Miller, A. Carrilero, S. Wall, F. J. García de Abajo, H. Altug, and V. Pruneri, "Ultrafast broadband tuning of resonant optical nanostructures using phase change materials," Adv. Opt. Mater. **4**(7), 1060-1066 (2016).
13. E. Petronijevic and C. Sibilia, "All-optical tuning of EIT-like dielectric metasurfaces by means of chalcogenide phase change materials," Opt. Express **24**(26), 30411-30420 (2016).
14. E. Petronijević, G. Leahu, V. Di Meo, A. Crescitelli, P. Dardano, E. Esposito, G. Coppola, I. Rendina, M. Miritello, M. G. Grimaldi, V. Torrisi, G. Compagnini, and C. Sibilia, "Near-infrared modulation by means of GeTe/SOI based metamaterial," Opt. Lett. **44**(6), 1508-1511 (2019).
15. M. Yang, Y. Yang, B. Hong, L. Wang, K. Hu, Y. Dong, H. Xu, H. Huang, J. Zhao, H. Chen, L. Song, H. Ju, J. Zhu, J. Bao, X. Li, Y. Gu, T. Yang, X. Gao, Z. Luo, and C. Gao, "Suppression of structural phase transition in VO_2 by epitaxial strain in vicinity of metal-insulator transition," Sci. Rep. **6**, 23119 (2016).
16. M. Dicken, K. Aydin, I. Pryce, L. Sweatlock, E. Boyd, S. Walavalkar, J. Ma, and H. Atwater, "Frequency tunable near-infrared metamaterials based on VO_2 phase transition," Opt. Express **17**(20), 18330- 18339 (2009).
17. M. D. Goldflam, T. Driscoll, B. Chapler, O. Khatib, N. Marie Jokerst, S. Palit, D. R. Smith, B-J. Kim, G. Seo, H-T. Kim, M. Di Ventra, and D. N. Basov, "Reconfigurable gradient index using VO_2 memory metamaterials," Appl. Phys. Lett. **99**, 044103 (2011).
18. J. Liang, X. Song, J. Li, K. Lan, and P. Li, "A visible-near infrared wavelength-tunable metamaterial absorber based on the structure of Au triangle arrays embedded in VO_2 thin film," J. Alloys Compd. **708**, 999-1007 (2017).
19. K. Appavoo, B. Wang, N. F. Brady, M. Seo, J. Nag, R. P. Prasankumar, D. J. Hilton, S. T. Pantelides, and R. F. Jr. Haglund, "Ultrafast phase transition via catastrophic phonon collapse driven by plasmonic hot-electron injection," Nano Lett. **14**(3), 1127−1133 (2014).
20. S. Lysenko, A. Rúa, V. Vikhnin, F. Fernández, and H. Liu, "Insulator-to-metal phase transition and recovery processes in VO_2 thin films after femtosecond laser excitation," Phys. Rev. B **76**, 035104 (2007).
21. D. G. Baranov, R. S. Savelev, S. V. Li, A. E. Krasnok, and A. Alù, "Modifying magnetic dipole spontaneous emission with nanophotonic structures," Laser Photonics Rev. 11(3), 1600268 (2017).
22. J. Li, N. Verellen, and P. V. Dorpe, "Enhancing magnetic dipole emission by a nano-doughnut-shaped silicon disk," ACS Photonics **4**(8), 1893−1898 (2017).
23. Q. Thommen and P. Mandel, "Left-handed properties of erbium-doped crystals," Opt. Lett. **31**(12), 1803-1805 (2006).
24. C. M. Dodson and R. Zia, "Magnetic dipole and electric quadrupole transitions in the trivalent lanthanide series: Calculated emission rates and oscillator strengths," Phys. Rev. B **86**, 125102 (2012).
25. B. Rolly, B. Bebey, S. Bidault, B. Stout, and N. Bonod, "Promoting magnetic dipolar transition in trivalent lanthanide ions with lossless Mie resonances," Phys. Rev. B **85**, 245432 (2012).
26. G. W. Bryant, F. J. García de Abajo, and J. Aizpurua, "Mapping the plasmon resonances of metallic nanoantennas," Nano Lett. **8**(2), 631–636 (2008).
27. J. Li, H. Guo, and Z. Li, "Microscopic and macroscopic manipulation of gold nanoantenna and its hybrid nanostructures," Photonics Res. **1**(1), 28-41 (2013).
28. L. Zhao, T. Ming, H. Chen, Y. Liang, and J. Wang, "Plasmon-induced modulation of the emission spectra of the fluorescent molecules near gold nanoantennas," Nanoscale **3**, 3849-3859 (2011).
29. X. Han, F. Zhao, K. He, Z. He, and Z. Zhang, "Near-perfect absorber of infrared radiation based on Au nanoantenna arrays," J. Nanophoton. **11**(1), 016018 (2017).
30. Y. Fan, C. Guo, Z. Zhu, W. Xu, F. Wu, X. Yuan, and S. Qin, "Monolayer-graphene-based broadband and wide-angle perfect absorption structures in the near infrared," Sci. Rep. **8**, 13709 (2018).
31. H. Kocer, S. Butun, B. Banar, K. Wang, S. Tongay, J. Wu, and K. Aydin, "Thermal tuning of infrared resonant absorbers based on hybrid gold-VO_2 nanostructures," Appl. Phys. Lett. **106**, 161104 (2015).
32. J. Pradhan, S. Anantha Ramakrishna, B. Rajeswaran, A. Umarji, V. Achanta, A. Agarwal, and A. Ghosh, "High contrast switchability of VO_2 based metamaterial absorbers with ITO ground plane," Opt. Express **25**(8), 9116-9121 (2017).
33. L. Yang, P. Zhou, T. Huang, G. Zhen, L. Zhang, L. Bi, X. Weng, J. Xie, and L. Deng, "Broadband thermal tunable infrared absorber based on the coupling between standing wave and magnetic resonance," Opt. Mater. Express **7**(8), 2767-2776 (2017).
34. Lumerical Solutions, Inc. http://www.lumerical.com/tcad-products/fdtd/
35. G. Leahu, E. Petronijevic, A. Belardini, M. Centini, R. Li Voti, T. Hakkarainen, E. Koivusalo, M. Guina, and C. Sibilia, "Photo-acoustic spectroscopy revealing resonant absorption of self-assembled GaAs-based nanowires," Sci. Rep. **7**, 2833 (2017).
36. T. Feng, Y. Zhou, D. Liu, and J. Li, "Controlling magnetic dipole transition with magnetic plasmonic structures," Opt. Lett. **36**(12), 2369-2371 (2011).
37. S. M. Hein and H. Giessen, "Tailoring magnetic dipole emission with plasmonic split-ring resonators," Phys. Rev. Lett. **111**(2), 026803 (2013).

38. M. Mivelle, T. Grosjean, G. W. Burr, U. C. Fischer, and M. F. Garcia-Parajo, “Strong modification of magnetic dipole emission through diabolo nanoantennas,” ACS Photonics **2**(8), 1071–1076 (2015).
39. R. Hussain, S. S. Kruk, C. E. Bonner, A. M. Noginov, I. Staude, Y. S. Kivshar, N. Noginova, and D. N. Neshev, “Enhancing Eu^{3+} magnetic dipole emission by resonant plasmonic nanostructures,” Opt. Lett. **40**(8), 1659-1662 (2015).
40. B. Choi, M. Iwanaga, Y. Sugimoto, K. Sakoda, and H. T. Miyazaki, “Selective plasmonic enhancement of electric- and magnetic-dipole radiations of Er ions,” Nano Lett. **16**(8), 5191-5196 (2016).
41. M. K. Schmidt, R. Esteban, J. J. Sáenz, I. Suárez-Lacalle, S. Mackowski, and J. Aizpurua, “Dielectric antennas - a suitable platform for controlling magnetic dipolar emission,” Opt. Express **20**(13), 13636-13650 (2012).
42. A. Vaskin, S. Mashhadi, M. Steinert, K. E. Chong, D. Keene, S. Nanz, A. Abass, E. Rusak, D. Y. Choi, I. Fernandez-Corbaton , T. Pertsch, C. Rockstuhl, M. A. Noginov, Y. S. Kivshar, D. N. Neshev, N. Noginova, and I. Staude, “Manipulation of magnetic dipole emission from Eu^{3+} with Mie-resonant dielectric metasurfaces,” Nano Lett. **19**(2), 1015–1022 (2019).
43. F. Kang, J. He, T. Sun, Z. Y. Bao, F. Wang, and D. Y. Lei, “Plasmonic dual-enhancement and precise color tuning of gold nanorod@SiO2 coupled core–shell–shell upconversion nanocrystals,” Adv. Funct. Mater. **27**(36), 1701842 (2017).